International Journal of Multiphase Flow 194 (2026) 105478

Contents lists available at ScienceDirect

International Journal of Multiphase Flow

journal homepage: www.elsevier.com/locate/ijmulflow

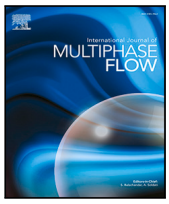

Research Paper

Effect of gas nuclei on the primary stage of shock–droplet interaction

Sotirios Damianos [a],*, Andreas Papoutsakis [b], Ioannis K. Karathanassis [a], Manolis Gavaises [a]

[a] Department of Mechanical Engineering and Aeronautics, School of Mathematics, Computer Science and Engineering, City St George's University of London, Northampton Square, EC1V 0HB, London, UK

[b] Department of Engineering, School of Physics Engineering and Computer Science (SPECS), University of Hertfordshire, College Lane Campus, AL10 9AB, Hatfield, UK

ARTICLE INFO

Keywords:
Cavitation
Shock propagation
Compressible multiphase flows
Phasic disequilibrium
Relaxation process

ABSTRACT

The presence of entrapped gas in liquids is well-documented, arising from gas solubility, surface irregularities, or prior phase-change events. In this study, simulations are carried out replicating an experiment involving a Mach 2.4 Planar shock interacting with a cylindrical water column, and the results are benchmarked against experimental pressure measurements in which the presence of entrapped air is reported. The liquid droplet is modelled as a homogeneous mixture of liquid and gas using a multiphase flow framework, and a novel relaxation approach is introduced to capture non-equilibrium effects within the mixture region. The effects of Gaseous Volume Fraction (GVF) and relaxation rate on shock attenuation, wave propagation speed, and cavitation are explored. The results reveal that increasing GVF enhances shock attenuation and slows down the wave propagation speed due to the mixture's higher compressibility. A non-monotonic relationship between relaxation rate and pressure peak intensity is observed, governed by the effect of the relaxation rate on shock diffusivity, with maximum attenuation occurring at intermediate rates. At high GVF, the low wave propagation speed leads to an interaction between the shocks formed internally and around the droplet, which suppresses the rarefaction wave formation. Regarding cavitation, results indicate that lower GVF promotes stronger gas growth due to less shock attenuation. Finally, this study provides a physical explanation for the temporal pressure variations reported in prior numerical works and highlights the critical role of entrapped gas in shock–droplet interaction dynamics.

1. Introduction

Shock–droplet interactions occur in a wide range of engineering configurations and natural environments. In the aerospace sector, these phenomena are encountered in high-speed flight through rain, such as atmospheric reentry vehicles (Ando, 2010; Kim and Hermanson, 2012), where raindrops interacting with shock waves under extreme conditions can lead to implications on structural integrity (Kondo and Ando, 2019; Marzbali and Dolatabadi, 2020; Moylan et al., 2013). In supersonic and hypersonic propulsion systems such as scramjets, ramjets, and rotating detonation engines, shock–droplet dynamics significantly influence fuel injection, atomisation and combustion processes (Liu et al., 2018; Meng and Colonius, 2015; Malik et al., 2022; Rossano and De Stefano, 2025; Viqueira-Moreira et al., 2023). Similarly, in liquid rocket engines, the interaction between shockwaves and injected propellant droplets is a key parameter for combustion efficiency (Song et al., 2023b). Automotive and heavy-duty engines equipped with high-pressure fuel injection systems also experience droplet velocities reaching supersonic regimes, leading to relevant shock interactions (Song et al., 2023a; Wei et al., 2023). Beyond traditional propulsion and mechanical systems, such interactions are exploited in biomedical contexts such as ultrasonic therapy (Coralic, 2015; Shpak et al., 2016; Johnsen and Colonius, 2009), and in advanced laser-based applications including bioprinting of 3D tissue structures (Kryou et al., 2021; Erfanian et al., 2024), controlled drug delivery (Sun et al., 2022), micromachining of hard materials (López López et al., 2016), laser cleaning (López López et al., 2017), and surface nanostructuring for nanolithography (Chang et al., 2016). Of particular interest to the present study is the primary stage of the interaction and the onset of cavitation within droplets upon shock impact, as this, can significantly alter interfacial dynamics and fragmentation processes.

Despite the extensive literature for droplet breakup regimes (Wierzba and Takayama, 1988; Joseph et al., 1999; Guildenbecher et al., 2009; Theofanous, 2011; Lee and Reitz, 2000; AalbVurg et al., 2003; Kékesi et al., 2014; Meng and Colonius, 2018; Theofanous and Li, 2008; Theofanous et al., 2012), experimental investigations into the initial phase of shock–droplet interaction remain scarce. Among

* Corresponding author.
E-mail address: Sotirios.Damianos@city.ac.uk (S. Damianos).

https://doi.org/10.1016/j.ijmultiphaseflow.2025.105478
Received 2 July 2025; Received in revised form 27 September 2025; Accepted 7 October 2025
Available online 10 October 2025

the limited studies available, Sembian et al. (2016) provided direct experimental evidence of cavitation occurring during the early stages of shock–droplet interaction. By confining the liquid between two parallel plates, resulting in a cylindrical water column and employing high-speed imaging and pressure transducers, they visualised and quantified the pressure wave dynamics within the liquid volume. Moreover, the formation of tension regions that triggered cavitation was identified. Similar observations have been reported in the context of droplet–wall impacts (Field et al., 1989, 2012; Obreschkow et al., 2011) where rapid deceleration and reflected waves also induce cavitation. Finally, (Liang et al., 2020) experimentally investigated water droplets embedded with a vapour cavity and observed the emergence of a transverse jet from the upstream interface, which impinged on the downstream interface. This highlighted the significant impact of the bubble's presence within the liquid droplet.

Several theoretical studies have been developed to investigate the complex wave dynamics in such configurations. Biasiori-Poulanges and El-Rabii (2021) used ray-tracing to model wave propagation within droplets, revealing time-dependent wavefront shapes characterised by cusp singularities formed through wave focusing, and providing parametric equations for confined wavefront surfaces. Building upon this framework, Xu et al. (2023) analysed the spatio-temporal evolution of planar, cylindrical converging, and diverging shocks. They showed that converging shocks intensify negative pressure zones and pressure oscillations, thereby increasing the likelihood of cavitation manifestation. Xiong et al. (2024) further refined these models using a multiphase solver coupled with ray-tracing, categorising the pressure evolution in 4 different stages: shock, fluctuation, relaxation, and expansion. Finally, it was shown that the location of the pressure wave focal point and the maximum negative pressure (NPP) point may diverge, particularly under high propagation speed differences between gas and liquid.

Turning to numerical studies, relevant 2D investigations are focusing on the primary stage of shock droplet interaction. Biasiori-Poulanges and Schmidmayer (2023) proposed a multi-material framework assuming heterogeneous cavitation, which incorporates the physical expansion of nuclei and phasic interactions parametrised by a relaxation rate. Their results demonstrated that pressure equilibrium models tend to overpredict cavitation intensity. Building upon this model, Schmidmayer and Biasiori-Poulanges (2023) showed that cavitation is inherently less probable to occur in spherical droplets than in cylindrical water columns. They further defined distinct regimes of cavitation intensity relative to shock strength. Specifically, exponential bubble growth was reported for Mach numbers below 4.38 and a linear growth for higher values; this was linked to the transition of the transmitted shock front from concave to convex. Besides, Jiao et al. (2024) examined how gas cavity size and eccentricity influence wave dynamics, jetting and cavity collapse, integrating real-fluid thermodynamics closure models. Despite these advances, 3D simulations with robust phase-change modelling remain scarce. Forehand et al. (2023) conducted one such study using a VOF solver, comparing two mass transfer models, revealing significantly enhanced wave focusing in 3D geometries but unrealistically low vapour formation. Finally, Nguyen et al. (2024) demonstrated that the onset of cavitation can alter the intensity of pressure waves following the reflection of the transmitted wave.

Despite the growing body of numerical studies on the primary stage of shock–droplet interactions, significant discrepancies remain between measured and simulated pressure fields, particularly regarding peak amplitudes, shock attenuation, and the arrival times of pressure waves at specific locations within the liquid volume. In their experimental campaign, Sembian et al. (2016) reported the presence of microbubbles within the liquid bulk during pressure measurements. While some studies account for nuclei within the droplet, their assumed concentrations are typically very low and serve merely as constraints within cavitation models, thereby failing to capture their potential influence on shock propagation (Forehand et al., 2023; Nguyen et al., 2024; Biasiori-Poulanges and Schmidmayer, 2023; Schmidmayer and Biasiori-Poulanges, 2023). Therefore, to date, no study has systematically investigated the role of dispersed gaseous phase within the liquid volume on the shock propagation in the primary stage of shock droplet interaction, despite it being a common phenomenon.

All liquids contain some dissolved gas, as they naturally absorb O_2, N_2, and CO_2 from the air according to Henry's law, and it is virtually impossible to completely eliminate them from any substantial liquid volume (Brennen, 2013). Shatalov et al. (2011) reported that air dissolved in water can form nano- and micro-bubbles, and that changes in external conditions can stimulate their emergence, growth, and coalescence. In a subsequent study, Shatalov et al. (2013) also stated that microbubbles spontaneously form in water, which under normal conditions contains approximately 2 vol% of dissolved gases. In addition, microbubbles can also originate from gas pockets trapped in surface crevices, rough textures, or on suspended particles such as dust or sediment (Scardina and Edwards, 2009). Repeated cavitation events can further contribute by releasing additional microbubbles into the liquid, effectively generating new nuclei (Bussonnière et al., 2020). Battistoni et al. (2015) and Gomez Santos et al. (2021) noted that liquid fuels often contain dissolved gases, which can flash out during pressure drops or the onset of cavitation. As a result, fuel and spray droplets may carry entrained gas, influencing their breakup and collapse dynamics. Giannadakis et al. (2008), also in the context of injection applications, reported that the initial gaseous volume fraction typically ranges from 0.01% to 0.5%. In spray cooling, Nguyen et al. (2024) experimentally demonstrated that droplets rebounding from a surface can encapsulate microscopic air bubbles, which subsequently oscillate and alter droplet behaviour. Similarly, Goyal et al. (2020) stated that raindrops can capture tiny air pockets during formation and impact. In biomedical ultrasonics and lithotripsy, gas nuclei are well documented and are known to significantly influence shock wave dynamics (Alavi Tamaddoni et al., 2019; Kung et al., 2020). Finally, in oversaturated conditions, droplets that have not yet vapourised may contain significant vapour volumes within the liquid bulk.

This is the first study investigating the effect of air, uniformly entrapped within the liquid volume, on wave propagation and cavitation dynamics during the initial stage of shock–droplet interaction. The form and topology of the air within the droplet are not explicitly resolved; instead, the air is assumed to exist at a subgrid scale and is modelled as a diluted phase forming a uniform mixture with the liquid phase. For the phasic interactions within this area, a novel relaxation approach is employed, which incorporates non-equilibrium dynamics in the system solution. The simulated pressure curves are compared with experimental measurements and other numerical studies, specifically in terms of peak amplitudes and wave speed. Particular emphasis is placed on the role of the relaxation rate, which defines the level of interaction between the two phases, and its influence on shock propagation for various conditions. In addition, the growth of the gaseous phase in response to the tension region is examined for various initial gas volume fractions. Finally, since entrapped air was also present in the experimental setup, this study offers a physical explanation for key discrepancies observed between numerical predictions and experimental pressure profiles.

2. Case description

The experimental configuration reported by Sembian et al. (2016) is adopted in this study. Specifically, a cylindrical water column with a diameter of 22 mm is assumed to interact with a Mach 2.4 shock wave, as illustrated in Fig. 1. Pressure measurements within the droplet have been obtained via two sensors positioned at 5 mm and 18 mm, respectively.

In the numerical simulations, these sensors are considered with a diameter of 5.54 mm, and pressure values are surface-averaged to align with the experimental measurement technique. Fig. 2(a) presents

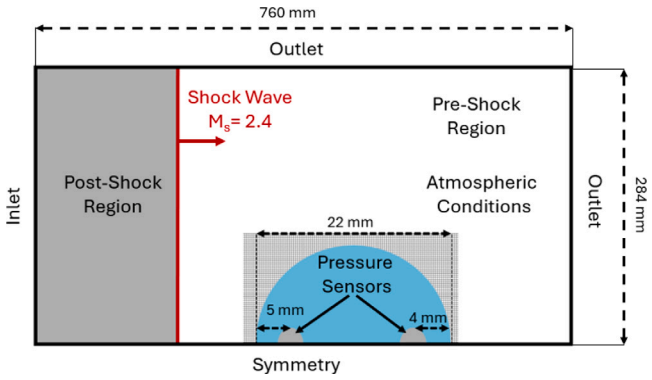

Fig. 1. Schematic representation of the investigated case. The background mesh shows the locations of the constant-length cells, which are later refined in the mesh-independence study.

a visualisation combining numerical schlieren images and pressure contours at the top and bottom of each panel, respectively. The former is used for tracking the shock front, while the latter for distinguishing compressive from expansive (rarefaction) waves. At the same time, Fig. 2(b) compares the pressure distribution as computed in the experimental results with recently published studies for this configuration (Sembian et al., 2016; Xu et al., 2023; Xiong et al., 2024; Forehand et al., 2023).

Once the shock impacts the droplet's surface, a compression wave is transmitted into the liquid, inducing an initial pressure rise at the location of the first sensor (1st Peak). The wave propagates and reaches the rear sensor, inducing a second pressure peak at $t = 13.75\,\mu s$ (2nd peak). At the same time, shock reflections form at the droplet's boundaries. As the transmitted shock reaches the rear of the droplet, it gives rise to a reflected wave that travels in the opposite direction. Due to the significant acoustic impedance difference between the droplet and the surrounding air, the droplet interface acts nearly as a perfect reflector, converting the incident shock into a rarefaction wave.

The droplet's concave geometry causes the rarefaction wave to focus at a specific point ($t = 20\,\mu s$), creating a significant pressure drop, which promotes cavitation (negative peak). The wave then reflects from this focal point and continues in a horseshoe pattern ($t = 22.5\,\mu s$), eventually reaching the first sensor location ($t = 27.5\,\mu s$), resulting in a local pressure drop. Finally, the wave reflects again at the droplet's front surface, now as a compression wave, and focuses near the first sensor, generating a third pressure peak ($t = 35\,\mu s$).

The distinct pressure peaks recorded by the sensors will be referred to hereafter as first, second, and third, according to their chronological occurrence. The first peak corresponds to the initial rise detected by the front sensor. The second peak represents the first rise at the rear sensor, while the third peak denotes the second rise at the front sensor, resulting from the second reflection of the wave. The negative peak refers to the tensile region formed near the rear sensor due to the focusing of the rarefaction wave.

Analysis of the numerical results presented in Fig. 2(b) reveals that all models capture the initial pressure peak with good accuracy. However, they tend to overestimate the magnitude of the second peak, indicating an underestimation of shock attenuation. This leads to an exaggerated prediction of the negative pressure peak and, consequently, unrealistic cavitation growth. Furthermore, a pronounced third peak is computed in simulations, which lacks experimental support. Finally, discrepancies in the timing of the second, third, and negative peaks are also evident.

3. Methodology

To simulate the shock-droplet interaction in the above configuration, an implementation of a Diffuse Interface Model (DIM) was used. To resolve the dynamic topology of the material interfaces as described by the DIM volume fraction, high-order interpolations and mesh refinement at the interfaces are employed. To this end, the Forest of oct-trees Adaptive Mesh Refinement (AMR) framework for unstructured hybrid meshes (Papoutsakis et al., 2020, 2018, 2014) was used. This approach allows for the on-the-fly refinement of the grid to self-similar cells to an arbitrary level. The connectivity of the elements, their genealogy, and their partitioning dynamically adapt to the emerging moving structures. Finally, the domain decomposition is dynamically balanced by deallocating and communicating spawn trees in new partitions.

Saurel's six-equation model (Saurel et al., 2009) is employed, which assumes velocity equilibrium between phases while allowing for pressure and thermal non-equilibrium effects. The approach extends the simplified five-equation framework (Kapila et al., 2001) to ensure positivity of the volume fraction, maintain a monotonic behaviour of the speed of sound, and address the derivation difficulties that arise when considering both phases (Pelanti and Shyue, 2014; Saurel et al., 2009). The model incorporates mass and energy conservation equations for each phase, a single momentum equation for the mixture and a transport equation for the volume fraction of the liquid phase. In addition, a seventh equation is solved to ensure conservation of the mixture's total energy. This equation addresses inconsistencies between the sum of the phasic energies and the total mixture energy, which arise from the non-conservative part of the phasic energy equations. The system of the governing equations written in vector form is given by:

$$\frac{\partial \mathbf{U}}{\partial t} + \nabla \cdot \mathbf{F}(\mathbf{U}) + \mathbf{H}(\mathbf{U}) \nabla \cdot \mathbf{u} + \mathbf{S}_{\mathbf{str}}(\mathbf{U}) = \mathbf{S}_{\mathbf{rlx}}(\mathbf{U}) \tag{1}$$

where $\mathbf{U}$ is the state vector, $\mathbf{F}$ is the flux vector, and $\mathbf{H}$ corresponds to the source terms arising from the non-conservative transport variables (i.e. volume fraction and phasic energy). The term $\mathbf{S}_{\mathbf{str}}$ accounts for the effect of the non-conservative stress tensor on phasic energy, while $\mathbf{S}_{\mathbf{rlx}}$ represents the source terms associated with the relaxation process, thus:

$$\mathbf{U} = \begin{bmatrix} a_1 \\ a_1\rho_1 \\ a_2\rho_2 \\ \rho_{\text{mix}}\mathbf{u} \\ a_1\rho_1 e_1 \\ a_2\rho_2 e_2 \\ \rho_{\text{mix}} E \end{bmatrix} \quad \mathbf{F} = \begin{bmatrix} 0 \\ a_1\rho_1\mathbf{u} \\ a_2\rho_2\mathbf{u} \\ \rho_{\text{mix}}\mathbf{u}\mathbf{u} + P\mathbf{I} - \boldsymbol{\tau} \\ a_1 e_1 \rho_1 \mathbf{u} \\ a_2 e_2 \rho_2 \mathbf{u} \\ (\rho_{\text{mix}} E + P)\,\mathbf{u} \end{bmatrix} \quad \mathbf{H} = \begin{bmatrix} -a_1 \\ 0 \\ 0 \\ 0 \\ a_1 P_1 \\ a_2 P_2 \\ 0 \end{bmatrix}$$

$$\mathbf{S}_{\mathbf{str}} = \begin{bmatrix} 0 \\ 0 \\ 0 \\ 0 \\ a_1\boldsymbol{\tau}_1 : \mathbf{u} \\ a_2\boldsymbol{\tau}_2 : \mathbf{u} \\ 0 \end{bmatrix} \quad \mathbf{S}_{\mathbf{rlx}} = \begin{bmatrix} \mathcal{P} \\ 0 \\ 0 \\ 0 \\ P_I\mathcal{P} + \mathcal{Q} \\ -(P_I\mathcal{P} + \mathcal{Q}) \\ 0 \end{bmatrix}$$

Here, a_k represents the volume fraction of phase k, $k = 1, 2$ $(a_1 + a_2) = 1$. The phasic density, pressure, and temperature are given by ρ_k, P_k and T_k, respectively. The phasic internal energy is expressed as $e_k = E_k - 1/2u^2$ where E_k is the total phasic energy. The mixture pressure, temperature, density and total Energy are given by $P = a_1P_1 + a_2P_2$, $T = a_1T_1 + a_2T_2$, $\rho_{\text{mix}} = a_1\rho_1 + a_2\rho_2$ and $E = a_1E_1 + a_2E_2$, respectively. Additionally, the velocity vector is represented as $\mathbf{u} = (u, v, w)$.

The stress tensor $\boldsymbol{\tau}$ is given by $\boldsymbol{\tau} = \mu\left[\nabla\mathbf{u} + (\nabla\mathbf{u})^T\right]$ where μ is the mixture viscosity defined as $\mu = a_1\mu_1 + a_2\mu_2$. The interfacial pressure P_I is defined as

$$P_I = \frac{Z_1P_1 + Z_2P_2}{Z_1 + Z_2} \tag{2}$$

where $Z_k = \rho_k C_k$ is the acoustic impedance and C_k is the speed of sound in phase k. The source terms $\mathcal{P}, \mathcal{Q}$ account for pressure and temperature non-equilibrium between phases. Finally, the mixture speed of

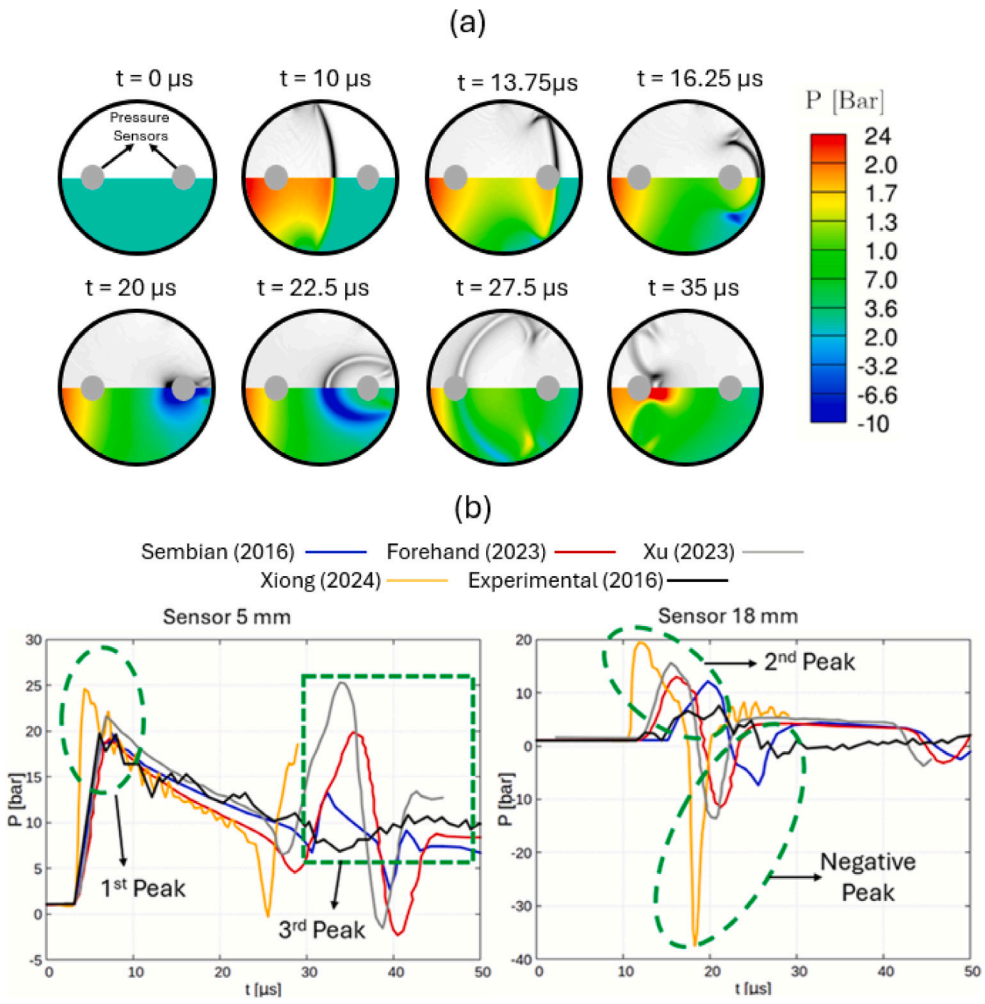

Fig. 2. (a) Numerical schlieren images (top half) and contour plots of the pressure field (bottom half) produced without cavitation model for the 22 mm water column. (b) Experimental pressure variation at each sensor (Sembian et al., 2016) compared against recent numerical predictions. The results from Xiong et al. (2024) are reported in locations having an offset of 0.5 mm from the sensor locations reported in the experiments.

sound is computed according to: $C = \sqrt{Y_1 C_1^2 + Y_2 C_2^2}$, where $Y_k = \frac{a_k \rho_k}{\rho_{\text{mix}}}$ is the mass fraction of phase k.

The system closure is obtained by specifying an Equation of State (EoS) for each phase, which establishes relationships among all thermodynamic quantities. Introducing the specific heat ratio γ_k and the constants η_k, and $P_{k,\infty}$, the Stiffened Gas (SG) EoS is written as:

$$P_k = (\gamma_k - 1)\,\rho_k e_k - \gamma_k P_{k,\infty} - (\gamma_k - 1)\,\eta_k \rho_k, \tag{3}$$

$$T_k = \frac{P_k + P_{k,\infty}}{C_{v,k}\rho_k\,(\gamma_k - 1)}, \tag{4}$$

$$C_k = \sqrt{\gamma_k \frac{P_k + P_{k,\infty}}{\rho_k}} \tag{5}$$

where $C_{v,k}$ is the heat capacity at constant volume for phase k. The SG EoS is employed for both phases, and the parameters used are summarised in Table 1, along with corresponding density and speed of sound at $P = 1.01\,\text{Bar}\,\&\,T = 300\,\text{K}$. Appendix A displays the suitability of SG EoS for capturing this phenomenon by comparing it with real EoS.

As this study investigates the effect of entrapped air within the liquid volume, a small amount of air is assumed to be initially present as a dispersed phase within the liquid, forming a uniform mixture. Its concentration is characterised by the Gaseous Volume Fraction (GVF), and the interaction between the two phases is modelled through the relaxation step described in Section 3.2.

The integration of the governing equations is achieved by an explicit density-based implementation. The numerical solution of the governing equations is achieved by employing the splitting procedure described by Saurel et al. (2009) in the following consecutive steps:

1. A hyperbolic step, i.e. solving Eq. (1) while neglecting $\mathbf{S_{rlx}}$ vector.
2. A relaxation step, where the source terms appearing in $\mathbf{S_{rlx}}$ are addressed and the energies of each phase are re-initialised according to the total energy of the system.

3.1. Hyperbolic step

In this stage, only the left-hand side of Eq. (1) is taken into account. For the conservative part, a finite volume Godunov scheme is applied (Godunov and Bohachevsky, 1959), extended to handle three-dimensional unstructured meshes. The HLLC approximate Riemann solver (Toro, 2013) is then employed at each cell boundary to define the perturbation state. At the same time, the non-conservative part of the equations is updated by approximating the volume integral with a mid-point rule and handling divergences through a centred scheme (Saurel et al., 2009). A second-order MUSCL approach (Chiapolino et al., 2017), suitably adapted for unstructured grids, is used to reconstruct the primitive variables at cell interfaces. Spatial gradients are evaluated using the Green–Gauss method, and the Minmode limiter (Sweby and

Table 1
Stiffened gas EoS constants, along with the corresponding density and speed of sound for the liquid and gaseous phases.

Phase k	P_∞	γ	η	ρ [kg/m^3]	C [m/s]
Liquid	5.102×10^8	4.4	-54.9×10^3	996.55	1501
Gaseous	0.00	1.4	0.00	1.174	347.5

Baines, 1984) is applied to preserve stability. Under these conditions, the state vector is updated as follows:

$$\mathbf{U}_i^{n+1} = \mathbf{U}_i^n + \frac{\Delta t}{V_i}\left(\sum_{f=1}^{N} A_f \mathbf{F}^* n_f + \sum_{f=1}^{N} A_f \left(\sum_{k=1}^{3} n_k \sum_{l=1}^{3} \left(\mathbf{H}_{ikl} + \mathbf{S}_{\mathbf{str},ikl}\right) u_l^*\right)\right) \tag{6}$$

where V_i, A_f, n_f are the volume, area and normal vector of face f belonging to cell i, respectively. The quantity u_l^* represents the flow velocity vector at the interface, while $\mathbf{F}_f^*$ denotes the perturbation state of the flux tensor, computed at the interfaces using the HLLC solver.

At this point, it is important to note that all quantities, except $\mathbf{S}_{\mathbf{str}}$, are discretised and computed in a conservative manner (Saurel et al., 2009). The non-conservative treatment of the term $\mathbf{S}_{\mathbf{str},i}$ does not affect the accuracy of our results, as it appears only in the phasic energy equations. These equations are later recomputed during the relaxation step in order to align with the conservative mixture energy. Therefore, at this stage, the computation of $\mathbf{S}_{\mathbf{str},i}$ serves merely as an initial estimation of energy before the relaxation step (Pelanti and Shyue, 2014). Finally, the temporal discretisation is extended to higher order through a 3rd order Runge–Kutta (RK) scheme (Jameson et al., 1981).

3.2. Relaxation step

The relaxation step addresses the right-hand side of Eq. (1). It captures mechanical and thermal non-equilibrium effects while ensuring consistency between the sum of the phasic energies and total mixture energy.

To maintain energy consistency across all computational stages, it is first necessary to correct discrepancies arising from the non-conservative equation of phasic internal energies. To this end, the energy residual is computed as $\Delta E = E_{tot} - a_1 e_1 - a_2 e_2 - 0.5(u^2 + v^2 + w^2)$ and the individual phase energies are updated according to: $e_k^{init} = e_k + \Delta E$. Unlike conventional methods, this correction is applied prior to the relaxation step and does not require pressure equilibrium, which is typically assumed in the literature (Saurel et al., 2009; Koukas et al., 2023; Bidi et al., 2022). As a result, the relaxation procedure remains energy-consistent while still permitting thermodynamic disequilibrium, as will be further explained.

When a shock wave propagates through a two-phase mixture of liquid and gas, it induces distinct thermodynamic states in each phase. However, due to interfacial interactions, the system evolves towards mechanical (pressure) and thermal (temperature) equilibrium. While many models assume this transition to be instantaneous (Saurel et al., 2009; Pelanti and Shyue, 2014; Koukas et al., 2023; Bidi et al., 2022), this assumption does not always hold. In reality, the system requires finite time to re-establish thermodynamic equilibrium following a disturbance, such as that caused by a shock wave.

To quantify the rate of this transition, we introduce two relaxation coefficients:

- μ: mechanical relaxation rate
- θ: thermal relaxation rate

These parameters characterise the responsiveness of each phase to interfacial imbalances. For example, as $\mu \to \infty$, mechanical equilibrium is achieved nearly instantaneously, indicating rapid pressure equalisation. In contrast, finite values of μ and θ reflect the physical time required for the system to return to equilibrium.

A further novelty introduced in this work lies in the integration of the relaxation processes. Traditionally, mechanical and thermal relaxation steps are performed sequentially. In contrast, this approach enforces both steps simultaneously within a single computational step. As demonstrated in Appendix B, this modification achieves comparable accuracy while significantly improving computational efficiency, robustness, and scalability. Finally, the method is designed to support arbitrary equations of state (EoS), ranging from neural network-based and tabulated EoS to simplified linear models, making it versatile and adaptable to a wide range of thermodynamic conditions.

In line with Schmidmayer et al. (2023), we begin by formulating the pressure evolution equations for each phase rather than using the energy conservation equations. Specifically

$$\frac{\partial P_1}{\partial t} = \frac{\rho_1 C_{I,1}^2}{a_1} \mu \Delta P \tag{7}$$

$$\frac{\partial P_2}{\partial t} = -\frac{\rho_2 C_{I,2}^2}{a_2} \mu \Delta P \tag{8}$$

where $C_{I,k}^2 = \frac{\frac{P_I}{\rho_k^2} - \frac{\partial e_k}{\partial \rho_k}\Big|_{P_k}}{\frac{\partial e_k}{\partial P_k}\Big|_{\rho_k}}$, and $\Delta P = P_2 - P_1$ is the pressure difference between gaseous and liquid phase following the hyperbolic step. Subtracting Eq. (7) from Eq. (8) yields:

$$\frac{\partial \Delta P}{\partial t} = -\left(\frac{\rho_2 C_{I,2}^2}{a_2} + \frac{\rho_1 C_{I,1}^2}{a_1}\right) \mu \Delta P \tag{9}$$

which represents an ODE in terms of the pressure difference ΔP. Assuming that the combined coefficient $\left(\frac{\rho_2 C_{I,2}^2}{a_2} + \frac{\rho_1 C_{I,1}^2}{a_1}\right)$ remains constant during relaxation, Eq. (9) admits the analytical solution:

$$\Delta P^* = \Delta P e^{-\left(\frac{\rho_1 C_{I,1}^2}{a_1} + \frac{\rho_2 C_{I,2}^2}{a_2}\right)\mu \Delta t} \tag{10}$$

where ΔP^* denotes the pressure difference after relaxation over a timestep Δt. Thus, with a properly defined relaxation rate μ, the pressure difference post-relaxation becomes a known quantity.

It is important to highlight that, following (Biasiori-Poulanges and Schmidmayer, 2023), the relaxation rate μ is assumed to be a function of the volume fractions. Therefore, the effective relaxation coefficient appearing in Eqs. (7)–(10) is essentially defined as $\mu(a_k) = a_1 a_2 \mu$, although, for brevity, it is denoted simply as μ. This formulation implies rapid relaxation for volume fractions near $a_k \sim 0.5$, i.e. at the shock droplet interface, and slower relaxation in regions where $a_K \to 0$, as in the bulk of a diluted two-phase mixture. Analogous expression to Eq. (10) can be derived for temperature, according to Pelanti (2022), leading to similar forms for ΔT^*, governed by the respective relaxation rate. However, due to the negligible influence of thermal effects within the liquid volume, we assume $\theta = \mu$, which does not compromise accuracy.

To determine the post-relaxation thermodynamic state, we consider the governing system as:

$$\Delta P^* = P_2^* - P_1^*, \tag{11}$$

$$\Delta T^* = T_2^* - T_1^*, \tag{12}$$

$$a_2^* = 1 - a_1^*, \tag{13}$$

$$\rho_2^* = a_2 \rho_2 \left(\frac{a_1 \rho_1}{\rho_1^*} - 1\right)^{-1}, \tag{14}$$

$$e_2^* = e_2 - a_1\rho_1 \frac{e_1^* - e_1}{a_2\rho_2}, \tag{15}$$

$$P_k^* = P(\rho_k^*, e_k^*), \tag{16}$$

$$T_k^* = T(\rho_k^*, e_k^*), \tag{17}$$

The superscript $(^*)$ denotes the values after the relaxation step. In addition, the last two equations correspond to the chosen equation of state (EoS), which defines pressure and temperature as functions of density and internal energy. The system has two unknowns: the density and energy of one phase (ρ_k^*, e_k^*), which are computed using a Newton–Raphson iterative method for solving nonlinear systems, as described below:

1. Start with estimates for ρ_1^* & e_1^*. Typically, these are the values obtained after the reinitialisation step.
2. Use Eqs. (14)–(15) to compute ρ_2^*&e_2^*.
3. Apply Eqs. (16) & (17) to compute P_k^*& T_k^* for both phases.
4. Define the residual vector $\mathbf{r} = (r_1, r_2)$ corresponding to Eqs. (11)–(12).
5. The gradients of the residuals (11)–(12) are computed numerically with respect to variables ρ_1 & e_1 by repeating steps 2-3 for $\rho_1 + \epsilon$ and $e_1 + \epsilon$, where $\epsilon \sim 10^{-4}$. Thus, the Jacobian can be defined as:

$$\mathbf{J} = \begin{bmatrix} \frac{\partial r_1}{\partial \rho_1} & \frac{\partial r_1}{\partial e_1} \\ \frac{\partial r_2}{\partial \rho_1} & \frac{\partial r_2}{\partial e_1} \end{bmatrix} \tag{18}$$

The update of the variables is computed as:

$$\mathbf{x}^{n+1} = \mathbf{x}^n - \alpha \mathbf{J}^{-1}\mathbf{r}, \qquad \mathbf{x} = (\rho_1^*, e_1^*)^T, \quad \mathbf{r} = (r_1, r_2)^T \tag{19}$$

where α is a relaxation factor. Finally, convergence is evaluated, and if not satisfied, steps 2-5 are repeated.

The volume fraction a_1^* is then determined from the phasic mass conservation. Under this assumption, cavitation appears as a heterogeneous phenomenon driven by the expansion of pre-existing nuclei rather than by mass transfer across phases. This assumption has also been used by Biasiori-Poulanges and Schmidmayer (2023) and is reported to work well compared with mass transfer models that tend to significantly underestimate the cavitated region (Forehand et al., 2023). Consequently, hereafter, references to cavitation will essentially denote gas growth; however, the term cavitation will still be used for clarity. Moreover, it is important to recall that the entrapped air is assumed to exist at a subgrid scale and is modelled as a diluted gas. In the initial condition, its volume fraction is considered constant across the liquid phase, forming a uniform mixture. As a result, no explicit bubble interfaces can be tracked within the droplet, which limits the representation of bubble collapse dynamics and the occurrence of secondary waves. Moreover, although the diffuse interface method typically thickens the interface, this is not expected to create significant issues. As explained, the only relevant interface in the modelling problem is that of the droplet–air boundary, which is represented with several levels of mesh refinement. Furthermore, due to the short duration of the phenomenon and the high inertia of the water droplet relative to air, this interface remains largely unaffected. Finally, the case under examination is modelled as a 2D column rather than a 3D droplet, to enable direct benchmarking against experimental data.

4. Results & discussion

In this section, we simulate the experiments conducted by Sembian et al. (2016) to examine the influence of entrapped air on the shock wave propagation. The pressure measurements are surface-averaged over a radius of 5.54 mm to align with the experimental measurement technique. To achieve a comprehensive understanding of the phenomenon, various relaxation rates are explored, and the corresponding physical mechanisms are explained. Finally, the impact of the initial GVF on cavitation dynamics is discussed.

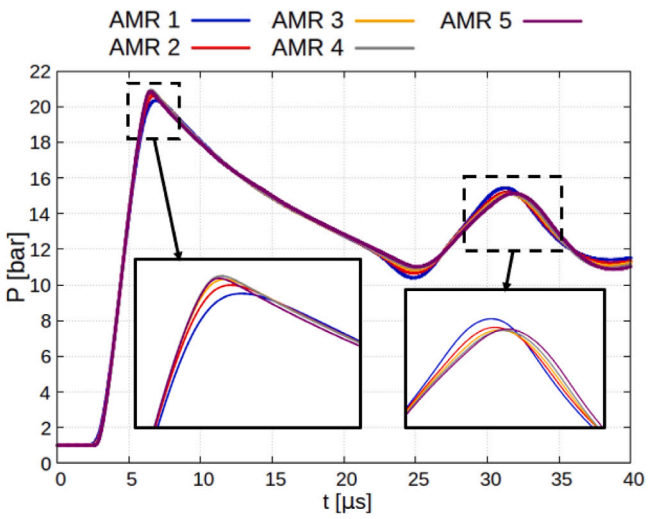

Fig. 3. Pressure variation over time at $x = 5$ mm for four mesh refinement levels applied around the liquid phase.

4.1. Mesh independence

A background mesh of 50 cells per diameter is used. Fig. 3 presents the pressure distribution computed using different Adaptive Mesh Refinement (AMR) levels around the liquid volume. Each sequential level of AMR decreases the cell size by a factor of 2 relative to the previous level, while AMR 1 represents the background mesh. The results indicate that four refinement levels are sufficient to obtain mesh independence, corresponding to a core cell size of $D/400$, where D is the water column diameter. The time step is set to $dt = 5\times10^{-9}$, equivalent to a CFL number of 0.155.

4.2. Effect of gaseous volume fraction

The effect of initial GVF is investigated under the assumption of infinite relaxation rate; this implies that both the gaseous and liquid pressure converge instantaneously to an equilibrium value. The range of initial GVF investigated is between $10^{-6} - 10^{-2}$. The lower bound is selected as a convergence point for low GVF in non-purified water, since it will be shown that it yields identical results as $GVF = 10^{-5}$. Determining the upper bound is less straightforward. For example, Shatalov et al. (2013) reports up to 2 vol% of dissolved gases in air, while Giannadakis et al. (2008) indicates that initial volume fractions for injection applications range from 0.01% to 0.5%. In general, if previous mass transfer events have occurred, or are occurring at the exact moment of shock interaction due to external conditions, the initial GVF in the droplet could easily exceed these reported values. To capture a broad range of possible scenarios, a maximum value of 10^{-2} is therefore considered. The results are presented in Fig. 4, where solid and dashed lines correspond to measurements from the first and second sensors, respectively.

It is evident that GVF significantly affects the temporal pressure distribution. While the first pressure peak remains largely unaffected, the second peak exhibits a high sensitivity, with larger values resulting in more pronounced attenuation. This behaviour stems from the presence of GVF, in which a portion of the shock energy is absorbed into compressing the gaseous phase. This energy transfer contributes significantly to shock attenuation.

Consequently, the first sensor, located close to the leading edge, does not yet register the energy absorption caused by the gaseous phase, and thus the first pressure peak remains nearly unchanged. In contrast, the second peak is substantially attenuated, as the shock wave has propagated further and more energy has been transferred. These

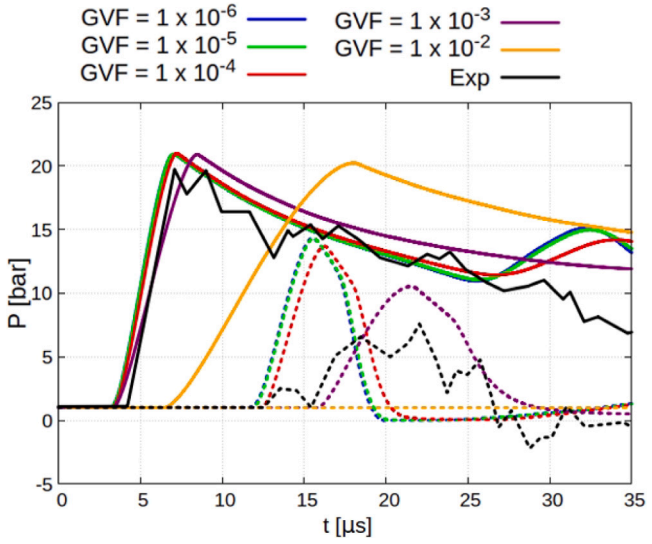

Fig. 4. Variation of mixture pressure over time for infinite relaxation rate ($\mu \to \infty$) and various gaseous volume fractions. Solid lines represent the sensor located at 5 mm, while dashed lines correspond to the sensor at 18 mm. The black lines indicate the experimental results reported by Sembian et al. (2016).

observations qualitatively agree with the experimental findings and explain the common overestimation in pressure amplitudes reported in other numerical simulations (Sembian et al., 2016; Xu et al., 2023; Xiong et al., 2024; Forehand et al., 2023). Moreover, the presence of GVF appears to influence the wave propagation speed and consequently affects the shock arrival time at each sensor. This trend is consistent with existing literature findings (Wijngaarden, 2007; Brennen, 2013), which report that increasing GVF enhances the compressibility of the mixture, thereby reducing the speed of sound. It also suggests that discrepancies in shock arrival times reported in prior studies may stem from neglecting these effects. Nonetheless, the discrepancy observed at the second sensor between numerical predictions and experimental results remains non-negligible, due to modelling simplifications and the assumption of an infinite relaxation rate which will be discussed in the next section.

4.3. Effect of relaxation rate

As GVF increases, the assumption of infinite relaxation rate no longer holds. The wave affects the pressure in each phase differently; thus, the liquid and gaseous phases should exhibit distinct pressures that gradually converge towards equilibrium. The finite relaxation rate μ is generally very challenging to determine experimentally. To address this, a wide range is initially considered, based on upper and lower convergence points. Subsequently, for specific GVFs, the analysis is refined to focus on the range that exhibits the highest interest.

Fig. 5 illustrates the influence of various relaxation rates for the previously considered GVF values. At this stage, the analysis is limited to $GVF \leq 1 \times 10^{-3}$, as higher values result in significant shock delays. These higher GVF cases involve distinct physical mechanisms and will therefore be examined separately in a following section. Following, focus is placed on evaluating the impact of the relaxation rate on four key parameters: (1) shock attenuation, (2) negative peak, (3) third peak, (4) wave propagation speed.

4.3.1. Shock attenuation

Shock attenuation manifests through the peak pressure difference between the first and the second sensor. From Fig. 5, it is evident that for very small GVFs ($GVF \leq 1 \times 10^{-4}$), the relaxation rate becomes practically irrelevant for the positive peaks. This is because the gaseous concentration is low enough to alter the shock energy, regardless of the assumed rate of energy absorption.

As GVF increases to $GVF = 1 \times 10^{-3}$, the level of shock attenuation starts becoming sensitive to the relaxation rate. This sensitivity arises from the increased capacity for energy exchange between phases, which amplifies the influence of the relaxation dynamics. To investigate this effect in greater detail, the results for $GVF = 1 \times 10^{-3}$ are replotted in Fig. 6 over a targeted range of relaxation rates that appear to have the most pronounced impact on pressure distribution and wave attenuation.

The variation in positive pressure peaks is governed by two main factors: the energy exchange between phases and the physical diffusivity of the shock front. The latter arises from the dynamic response of the gaseous phase to pressure fluctuations and is the primary mechanism for shock attenuation, as will be demonstrated in the discussion relevant to Fig. 7. In the limit of infinite relaxation rates (blue line), although the energy exchange is maximised, the system behaves like a homogenised fluid, rapidly reaching pressure equilibrium. This leads to minimal diffusivity and, consequently, a sharp shock front characterised by a high peak pressure.

As the relaxation rate decreases (red, yellow & grey lines), the gaseous phase is unable to instantaneously adapt to changes in pressure. Instead, it lags behind the compression wave, resisting compression, which enhances local pressure gradients, increases energy dissipation, and promotes wave spreading. Although the energy absorption does not change significantly, the increased energy dispersion reduces the pressure peaks. Finally, in the limit of vanishing relaxation rates (purple & green lines), the liquid phase no longer perceives the presence of gas, and the system behaves as a single-phase flow with negligible energy exchange. This leads to the reappearance of a sharp shock and very high-pressure peaks. Remarkably, a diffuse region is also observed in the experimental data (red arrow), justifying the presence of GVF within the water column.

The lower part of Fig. 7 presents the shock fronts for $GVF = 1{\times}10^{-6}$, confirming that the gaseous volume fraction is too low to significantly affect wave propagation or its attenuation. The shock front remains sharp regardless of the relaxation rate, resulting in consistently high pressure peaks.

Table 2 summarises the variations in peak pressures and shock attenuation as a function of both relaxation rate and GVF, highlighting the non-monotonic behaviour of pressure peaks with respect to the relaxation rate. This behaviour arises from the critical influence of the gas volume fraction (GVF) and the relaxation rate on shock propagation and attenuation, governed by shock diffusivity and interphase energy exchange. These effects vary markedly from case to case, as discussed previously. For $GVF \leq 1{\times}10^{-4}$, a single average value is reported across all relaxation rates due to the minimal sensitivity of the pressure peak in this regime. The table also includes deviations from experimental values, showing close agreement at the first sensor location across most cases, but substantial discrepancies at the second peak. Among the investigated cases, results for $GVF = 1 \times 10^{-3}$ demonstrate the best alignment with experimental results.

4.3.2. Negative peak

Figs. 5 and 6 clearly demonstrate that the relaxation rate also has a significant impact on the negative pressure peak. The negative peak is of high importance, as it is closely associated with the intensity of cavitation. The mechanism governing here can be conceptualised through the shock fronts focusing on the reflection wave, as presented in Fig. 8 for $GVF = 1 \times 10^{-3}$ and $GVF = 1 \times 10^{-6}$.

At high relaxation rates ($\mu \to \infty$), the negative pressure peak completely disappears, regardless of the GVF. This behaviour is attributed to the intense energy exchange between the two phases. Specifically, the rarefaction wave has a much stronger effect on the liquid phase due to its low compressibility, causing a significant drop in liquid pressure (up to an order of 100%–200%), while the gas phase pressure decreases

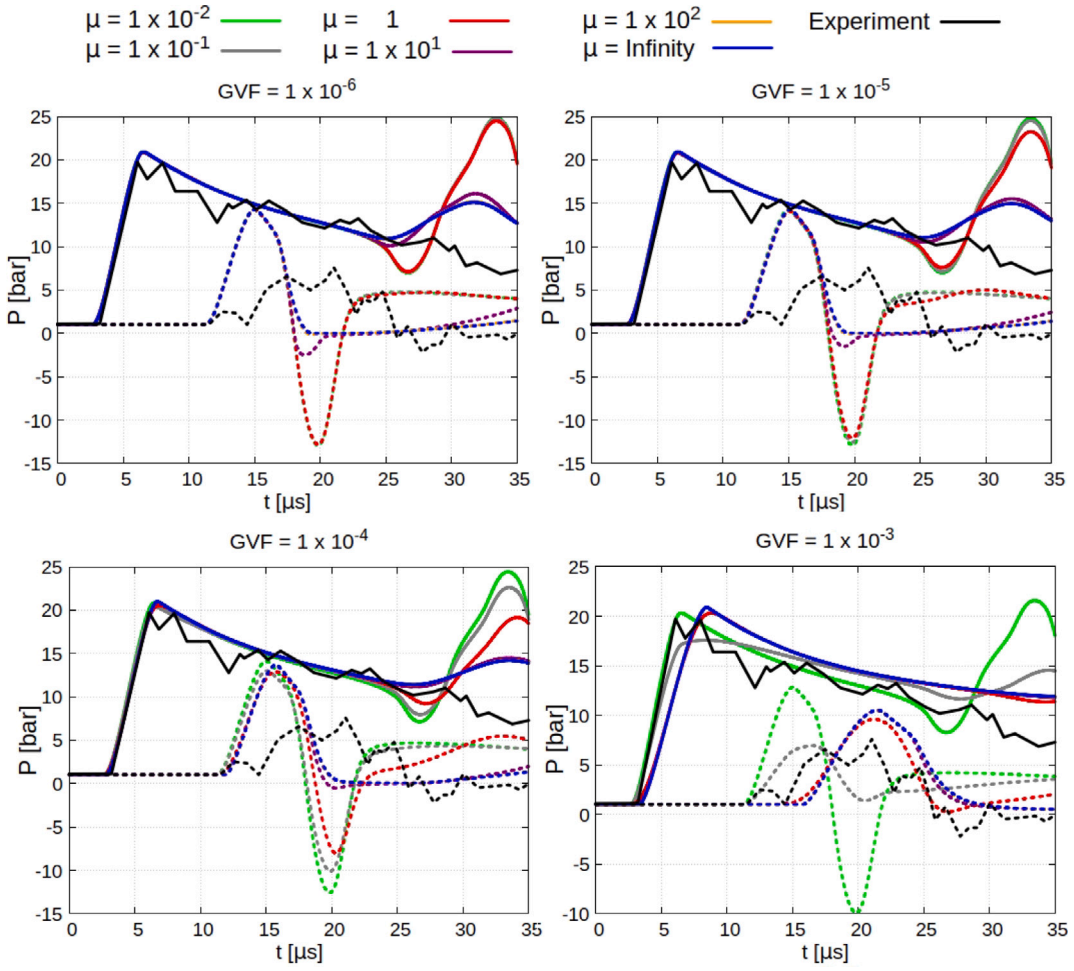

Fig. 5. Variation of mixture pressure over time for various relaxation rates μ. Each plot represents a different initial gaseous volume fraction (GVF) within the droplet. Solid lines represent the sensor located at 5 mm while dashed lines represent the sensor located at 18 mm. The black lines represent the experimental results of Sembian et al. (2016). (For interpretation of the references to colour in this figure legend, the reader is referred to the web version of this article.)

Table 2
Summary of peak pressures at 5 mm and 18 mm, their respective deviations from experimental values ($P_{5\text{mm}} = 19.60\,\text{bar}$ & $P_{18\text{mm}} = 7.89\,\text{bar}$) , and the overall shock attenuation, expressed as a function of the first peak pressure $\left(\frac{P_{5\text{mm}}-P_{18\text{mm}}}{P_{5\text{mm}}}\%\right)$. The experimental attenuation is $Att_{exp} = 59.74\%$. For small GVF values, average values are reported, together with their maximum deviations due to negligible differences.

GVF	μ	$P_{5\text{mm}}$ [Bar]	$P_{18\text{mm}}$ [Bar]	$\Delta P_{5\text{mm}}$[%]	$\Delta P_{18\text{mm}}$[%]	Att. [%]
1×10^{-6}	Avg	20.90 (±0.1)	14.32 (±0.08)	6.63 (±0.5)	81.50 (±1.0)	31.48 (±1.0)
1×10^{-5}	Avg	20.85 (±0.15)	14.21 (±0.2)	6.38 (±0.7)	80.10 (±2.4)	31.84 (±1.2)
1×10^{-4}	Avg	20.60 (±0.4)	13.24 (±1.0)	5.10 (±1.9)	67.80 (±13.1)	35.72 (±4.9)
	0.01	20.32	12.81	3.67	62.36	36.95
	0.05	18.53	8.99	−5.46	13.94	51.48
1×10^{-3}	0.25	17.57	6.94	−10.35	−12.04	60.50
	0.5	19.60	8.305	0.00	5.26	57.62
	1.0	20.32	9.59	3.67	21.54	52.80
	∞	20.91	10.52	6.63	33.33	49.67

only slightly (∼ 5%). However, under the assumption of instantaneous relaxation, the pressures of both phases must rapidly converge to a common equilibrium. As a result, the liquid pressure pulls down the gas pressure, leading to a substantial increase in the gas volume fraction. This mechanism gives rise to an extensive cavitation region, which completely attenuates the shock wave, due to high energy exchange between the two phases, irrespective of the initial GVF.

For medium range relaxation rates ($0.1 \leq \mu \leq 1$) and a non-negligible amount of GVF ($GVF \geq 1\times10^{-3}$) the negative pressure peak remains absent. However, a different behaviour compared to larger relaxation rates is observed here. At these relaxation rates, the shock front lies within a diffusive regime and can be conceptualised as consisting of multiple shock layers. When the first layer reflects, it encounters subsequent layers, leading to mutual cancellation. As a result, only a small fraction of the energy escapes, producing a very weak rarefaction wave.

Finally, at very small relaxation rates, the energy exchange between phases diminishes, causing the shock front to sharpen once again, regardless of the GVF. Gaseous expansion no longer occurs due to the insufficient phase interaction. The rarefaction wave propagates undisturbed, and its amplitude becomes primarily governed by the shock energy left following the second positive peak. Consequently, as

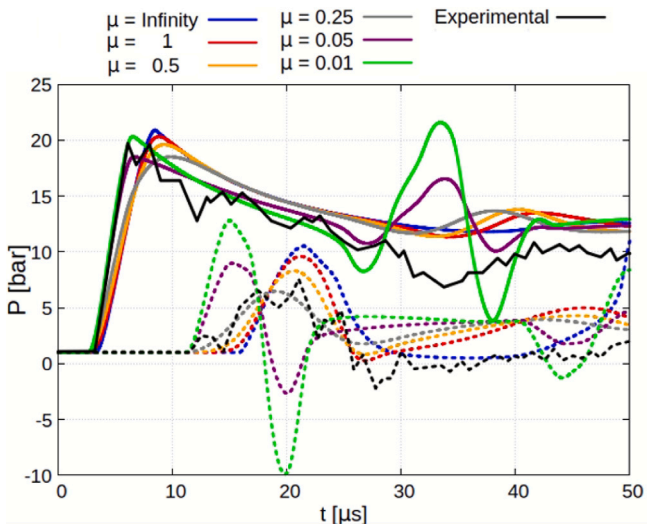

Fig. 6. Variation of mixture pressure over time for $GVF = 1 \times 10^{-3}$ and various relaxation rates. Solid lines represent the sensor located at 5 mm while dashed lines represent the sensor located at 18 mm. The black lines represent the experimental results of Sembian et al. (2016). (For interpretation of the references to colour in this figure legend, the reader is referred to the web version of this article.)

the relaxation rate decreases, the magnitude of the negative pressure peak increases.

4.3.3. Third peak

The third pressure peak primarily depends on the shock energy remaining after the wave reflection. It is evident that in scenarios involving significant energy exchange during propagation and reflection, the peak is nearly absent, which is in agreement with the experimental results. In contrast, at very low relaxation rates, its intensity becomes unrealistically high compared to experimental observations.

4.3.4. Propagation speed

Figs. 5 and 6 show that the relaxation rate also affects the arrival time of the wave in each sensor and thus the propagation speed. This effect stems from the impact of the relaxation rate on the compressibility of the mixture. Specifically, at high relaxation rates, gas compression is promoted, causing the mixture to behave more like a compressible medium, which in turn reduces the speed of sound. Conversely, at low relaxation rates, gas compression is significantly limited, and the mixture tends to behave more like an incompressible fluid, resulting in an increased speed of sound.

Table 3 summarises the variations in propagation speed, calculated based on the travel time between Sensor 1 and Sensor 2. Results for $GVF = 1 \times 10^{-2}$ are also included and will be discussed in the following section. It is evident that for constant GVF, the relaxation rate can decrease the propagation speed by up to an order of 70%.

4.3.5. High GVF values

As previously discussed, high GVF values lead to distinct physical behaviours compared to lower GVF scenarios. Fig. 9 illustrates the temporal pressure variation for a GVF of 1×10^{-2}. Notably, substantial time delays are observed in both the first and second pressure peaks for relaxation rates $\mu > 0.1$, which are attributed to the pronounced impact of high GVF on the mixture's compressibility, as explained in the previous section. Another notable difference lies in the amplitude of the second peak, which remains unexpectedly high under these conditions.

To clarify this phenomenon, Fig. 10 presents the shock fronts alongside pressure contours for $\mu = 10$. Due to the extremely low propagation

Table 3
Propagation speed variation for various relaxation rates and GVF calculated based on the travel time between Sensor 1 and Sensor 2. ΔC signifies the percentage difference from the nominal speed of sound for GVF = 1×10^{-6}. For small GVF values, average values are reported, together with their maximum deviations due to negligible differences.

GVF	μ	C [m/s]	ΔC[%]
1×10^{-6}	Avg	1511 (±0.0)	0.0
1×10^{-5}	Avg	1510 (±0.0)	0.0
1×10^{-4}	Avg	1460 (±50.0)	3.3 (±3.3)
1×10^{-3}	0.01	1508	0.2
	1	996	34.1
	10	996	34.1
1×10^{-2}	0.01	1391	7.9
	1	452	70.1
	10	433	71.3

speed inside the liquid bulk (~ 450 m/s), the external shock wave propagates faster (~ $2.4 \times 340 = 816$ m/s), giving the shock front a concave shape (a-c), a feature also reported by Schmidmayer and Biasiori-Poulanges (2023) and Xu et al. (2023). Once the external shocks reach the rear of the droplet, they collide and a new compression wave is generated (d). This wave is transmitted to the still unaffected part of the droplet (e) and propagates in the opposite direction of the initial internal shock. When these two compression waves collide (f), they produce a strong secondary pressure peak (g) and suppress the formation of a rarefaction wave. Hence, although the initial shock attenuates as expected, the delayed interaction leads to a secondary shock formation that significantly amplifies the pressure. Finally, as the relaxation rate decreases, the governing behaviour gradually re-aligns with the patterns discussed in earlier sections.

4.4. Cavitation dynamics

The influence of the GVF and shock attenuation on cavitation is presented in this section. Cavitation depends on two key parameters: the magnitude of the rarefaction wave, which itself depends on the attenuation of the initial shock, and the degree of interaction between the two phases. The latter is directly related to the relaxation rate and the effect that low liquid pressures have on gaseous expansion. Based on comparisons between experimental and numerical results for the shock attenuation and wave speed, the relaxation rate, which properly reflects the physical behaviour of the system, should lie within the range of $\mu = 0.5$ to $\mu = 4.0$. Thus, a relaxation rate of $\mu = 2$ is selected as representative and can be generalised across the entire range.

To compare the cavitating regions across cases, the results are normalised by the initial gaseous volume, allowing the evaluation of a compression/expansion ratio for the gaseous phase in the investigated area. Fig. 11(a) presents the Volume Ratio (VR) for various GVF in the location of the second sensor, while Fig. 11(b) shows the contour plots of the volume ratio for the whole liquid volume. It is evident that as the initial GVF decreases, the VR increases, with an approximate fivefold scaling between successive GVF levels. Notably, even when comparing $GVF = 1 \times 10^{-6}$ with $GVF = 1 \times 10^{-5}$, where the rarefaction intensity is nearly identical, a significant difference in VR is observed. This indicates that the expansion ratio of the gaseous phase strongly depends on the absolute initial GVF value.

It is important to clarify that, in absolute terms, the cavitating gaseous volume remains larger in increasing GVF cases. However, in this analysis, we select to quantify cavitation through the Volume Ratio, which reveals that lower initial GVFs undergo more intense relative expansion. Finally, for high initial GVF values ($GVF \geq 1 \times 10^{-3}$), cavitation is absent due to the strong attenuation of the rarefaction wave.

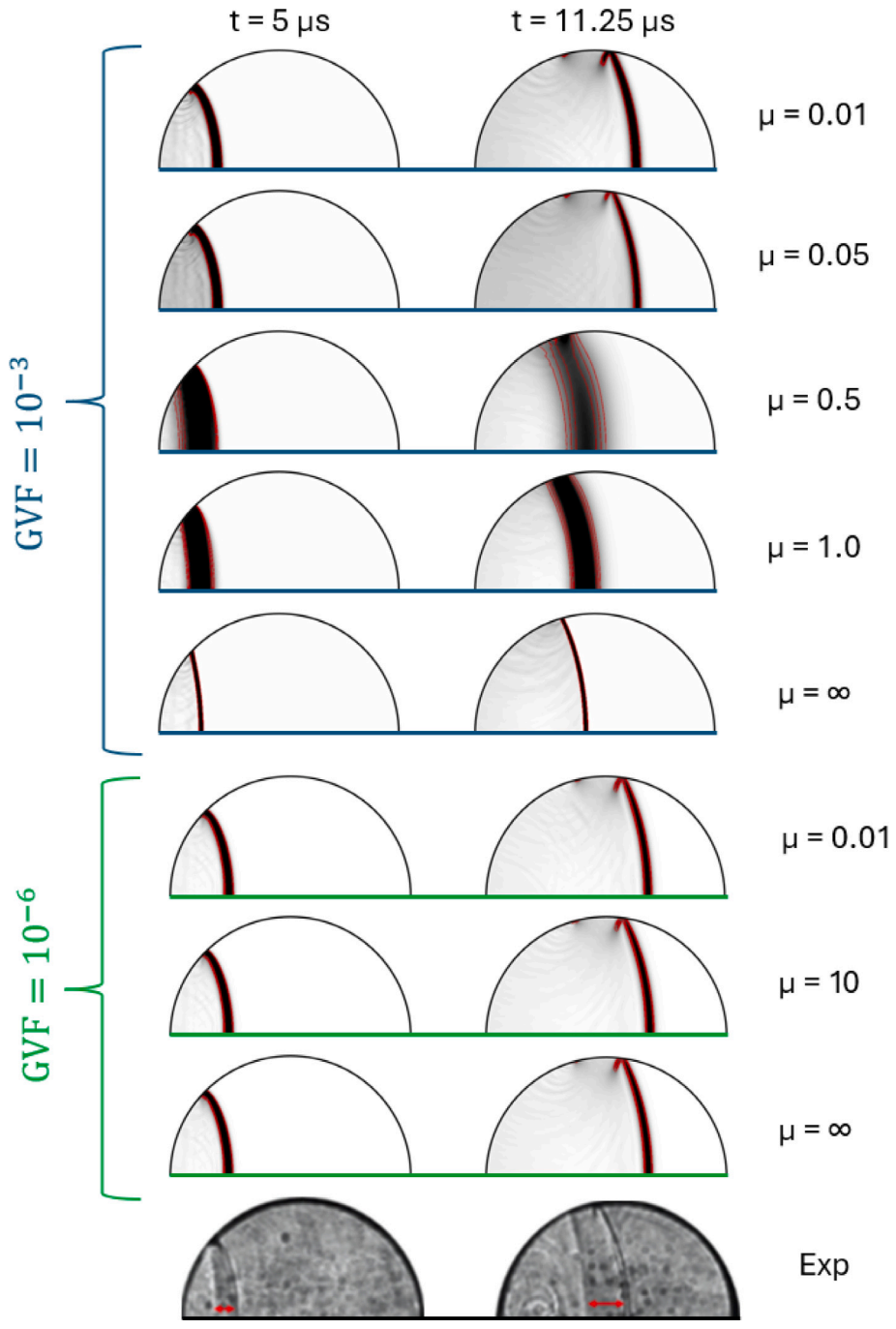

Fig. 7. Shock visualisation for different relaxation rates with initial GVF $= 1 \times 10^{-3}$ (upper part) and $GVF = 1 \times 10^{-6}$ (lower part). Red lines represent iso-lines of constant density gradient and highlight the diffusivity of the shock. Different relaxation rate values are used for each GVF to highlight the distinct regimes of each case. (For interpretation of the references to colour in this figure legend, the reader is referred to the web version of this article.)

5. Conclusion

In this study, Saurel's six-equation model was adopted to investigate the impact of GVF during the initial stage of shock-droplet interaction. In addition, a novel finite-rate relaxation approach was developed to assess the response of the gaseous phase induced by shock wave propagation through the liquid phase.

The findings show that GVF enhances shock attenuation by requiring additional energy to compress the gas phase, while also reducing the shock propagation speed due to increased mixture compressibility. Shock attenuation is negligible for GVF values below 10^{-4}, but becomes increasingly significant at higher concentrations, where the relaxation rate plays a key role. In this regime, shock diffusivity dominates, leading to maximum attenuation at intermediate relaxation rates.

The amplitude of the negative pressure peak, linked to cavitation intensity, is also governed by the relaxation rate. At high GVF, rarefaction waves are weakened either by strong cavitation under fast relaxation or by enhanced diffusivity at moderate rates. At low GVF, fast relaxation still suppresses rarefaction, but slower rates result in more intense rarefaction and, consequently, stronger cavitation.

Discrepancies between experimental and numerical pressure profiles, particularly the third peak, are attributed to shock attenuation effects introduced by GVF, which were often neglected in previous models. The relaxation rate further affects the effective speed of sound

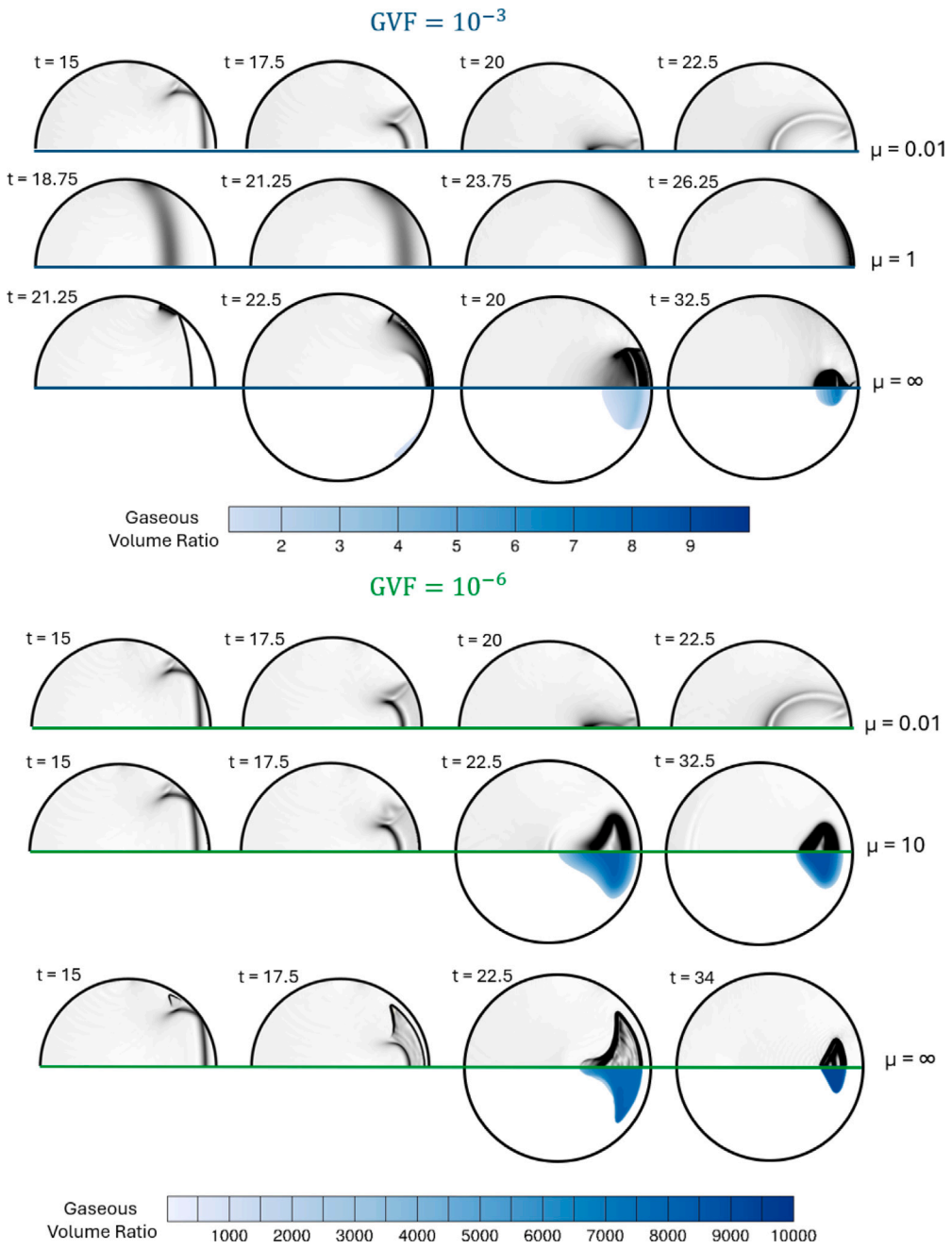

Fig. 8. Shock visualisation highlighting the reflected wave under varying relaxation rates, for initial GVF of 1×10^{-3} (top) and 1×10^{-6} (bottom). The lower half of each frame illustrates the gaseous volume ratio, representing the instantaneous GVF normalised by its initial value, and is displayed only when cavitation occurs. Different relaxation rate values are used for each GVF to highlight the distinct regimes of each case. Note that different colour scales are employed for the two GVF cases to account for their distinct dynamic ranges. Time is in μs.

in the mixture, with higher rates leading to greater compressibility and slower wave propagation. At sufficiently high GVF ($\geq 10^{-2}$), this reduction in shock speed may cause compression waves to collide, effectively suppressing rarefaction wave formation. Moreover, lower GVF levels are found to promote more intense cavitation due to weaker attenuation and more vigorous gaseous expansion. Overall, these factors highlight the crucial influence of gaseous impurities in the primary stage of shock–droplet interactions and explain why conventional approaches failed to capture the pressure curves reported in the experimental campaign of Sembian et al. (2016), thereby contributing new insights to the field.

Although the scope of this research is primarily aimed at providing a broader perspective on the combined effect of the initial GVF and the relaxation rate in shock–droplet dynamics, instead of defining the GVF in Sembian et al. (2016) experimental campaign, the authors suggest that the most reliable way to determine the GVF is by analysing the propagation speed and pressure peaks. In this case, the best agreement was obtained for $GVF = 10^{-3}$ and for μ values ranging from 0.2 to 2. This range of μ also aligns closely with the values proposed by Biasiori-Poulanges and Schmidmayer (2023), despite being derived through a completely different approach. However, each case has its own specific factors, so this solution should not be generalised to other cases.

Future studies could extend this framework to three-dimensional geometries and adopt more advanced relaxation models that explicitly account for gas in the form of discrete bubbles. Such models would be

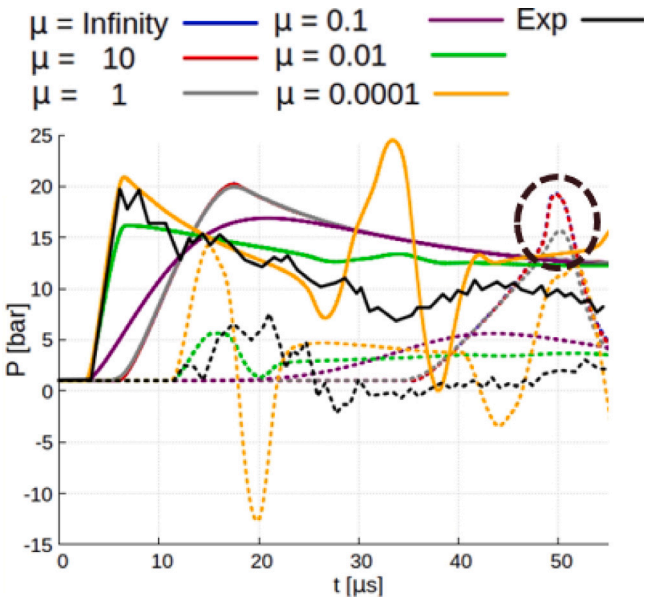

Fig. 9. Variation of mixture pressure over time for $GVF = 1 \times 10^{-2}$ and various relaxation rates. Solid lines represent the sensor located at 5 mm while dashed lines represent the sensor located at 18 mm. The black lines represent the experimental results of Sembian et al. (2016). (For interpretation of the references to colour in this figure legend, the reader is referred to the web version of this article.)

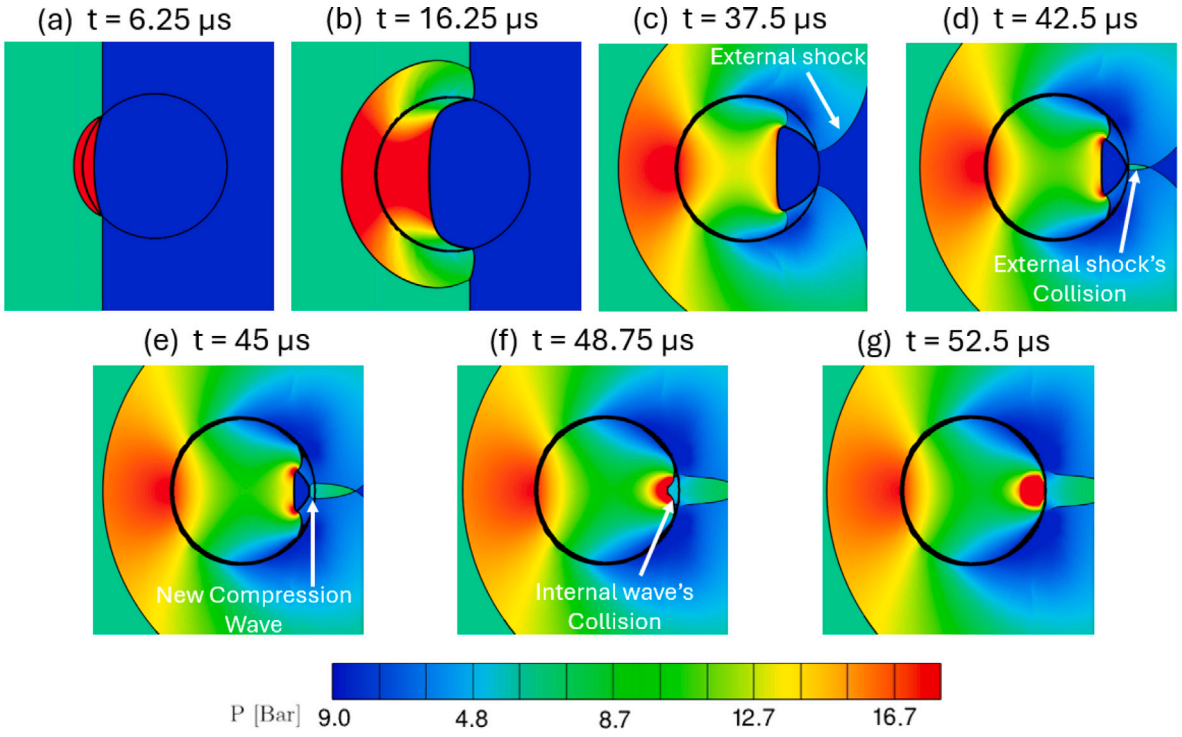

Fig. 10. Temporal evolution of pressure contours for $\mu = 10$ and initial GVF of 1×10^{-2}. The black line represents density gradients higher than 4000 to visualise the droplet boundaries and the shock front. (For interpretation of the references to colour in this figure legend, the reader is referred to the web version of this article.)

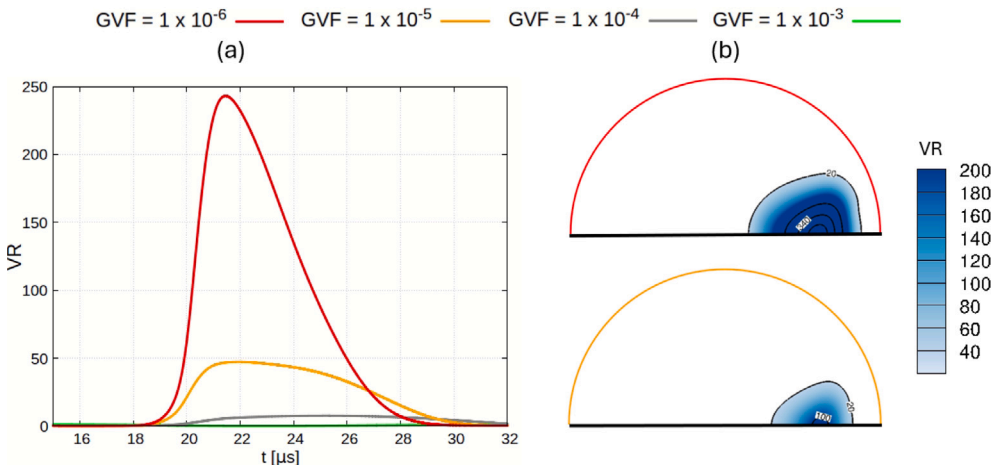

Fig. 11. (a) Comparison of the Volume Ratio (VR), defined as the instant gaseous volume to the initial gaseous volume at the location of the second sensor and (b) contours together with iso-lines of the VR at $t = 22.5\,\mu s$ for GVF $= 1 \times 10^{-6}$ and GVF $= 1 \times 10^{-5}$. The droplet interface colour align with the GVF label.

better equipped to capture bubble oscillations and the secondary shocks they emit when subjected to incident shock waves.

CRediT authorship contribution statement

Sotirios Damianos: Writing – original draft, Visualization, Validation, Software, Methodology, Investigation, Formal analysis, Data curation, Conceptualization. **Andreas Papoutsakis:** Writing – review & editing, Supervision, Software, Conceptualization. **Ioannis K. Karathanassis:** Writing – review & editing, Supervision, Methodology, Conceptualization. **Manolis Gavaises:** Writing – review & editing, Supervision, Resources, Project administration, Funding acquisition, Conceptualization.

Declaration of competing interest

The authors declare that they have no known competing financial interests or personal relationships that could have appeared to influence the work reported in this paper.

Acknowledgements

This work was supported by the Horizon Europe MSCA DN project with acronym MFLOPS, Grant Agreement No. 101072851. Additional funding has been received by the UK's Research and Innovation Council (UKRI) through grant EP/X041387/1. Views and opinions expressed are however those of the author(s) only and do not necessarily reflect those of the European Union or European Research Executive Agency (REA). Neither the European Union nor the granting authority can be held responsible for them.

Appendix A. Comparison of real EoS with SG EoS

This appendix presents a comparison of the pressure distribution over time at each sensor, computed using either the simplified stiffened gas (SG) equation of state (EoS) or a real EoS, to evaluate the suitability of the SG EoS. The parameters for the SG EoS are taken as described in Table 1. For the real EoS, a tabulated approach is employed. Specifically, thermodynamic data are generated using the REFPROP software in the form of structured tables, as functions of density and internal energy for both phases. A 200×50 table is used for water, covering a density range of 996 to $1000\ \mathrm{kg/m^3}$ and internal energy from $74,807$ to $91,651\ \mathrm{J/kg}$. For air, a 400×600 table is generated, with density ranging from 0.34 to $60.62\ \mathrm{kg/m^3}$ and internal energy from $322,861$ to $718,866\ \mathrm{J/kg}$. Fig. 12 compares the results from both approaches, demonstrating that the simplified SG equation of state effectively captures the pressure variations associated with shock wave propagation.

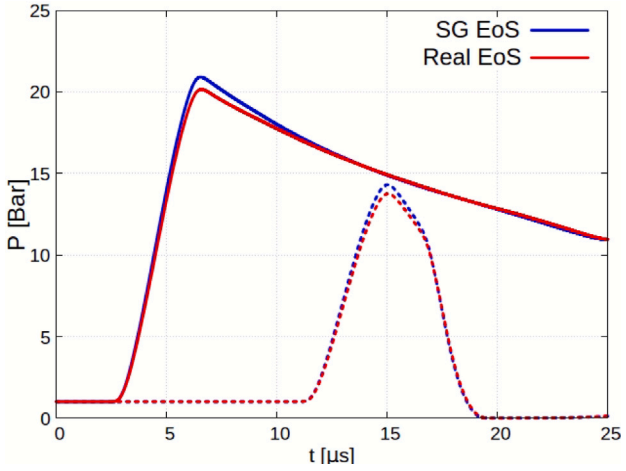

Fig. 12. Variation of mixture pressure over time for real and simplified (SG) equation of state. Solid lines represent the sensor located at 5 mm, while dashed lines correspond to the sensor at 18 mm.

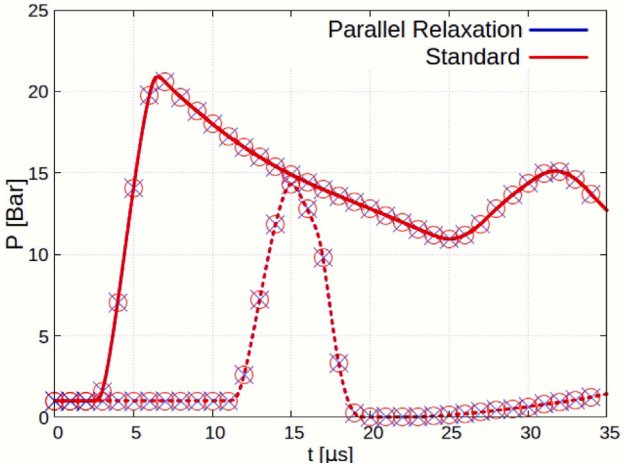

Fig. 13. Variation of mixture pressure over time for the two relaxation approaches. Solid lines represent the sensor located at 5 mm, while dashed lines correspond to the sensor at 18 mm.

Appendix B. Comparison of standard relaxation approach with parallel relaxation

This appendix aims to prove that the proposed approach for the relaxation step produces similar results to the standard approach as described in Saurel et al. (2009), Pelanti and Shyue (2014). Fig. 13 compares these two approaches, verifying that the results are identical.

Data availability

Data will be made available on request.

References

AalbVurg, C., Van Leer, B., Faeth, G.M., 2003. Deformation and drag properties of round drops subjected to shock-wave disturbances. AIAA J. 41 (12), 2371–2378.

Alavi Tamaddoni, H., Roberts, W.W., Hall, T.L., 2019. Enhanced shockwave lithotripsy with active cavitation mitigation. J. Acoust. Soc. Am. 146 (5), 3275–3282. http://dx.doi.org/10.1121/1.5131649.

Ando, K., 2010. Effects of Polydispersity in Bubbly Flows (Ph.D. thesis). California Institute of Technology.

Battistoni, M., Duke, D., Swantek, A., Tilocco, F., Powell, C., Som, S., 2015. Effects of noncondensable gas on cavitating nozzles. At. Sprays 25, 453–483. http://dx.doi.org/10.1615/AtomizSpr.2015011076.

Biasiori-Poulanges, L., El-Rabii, H., 2021. Shock-induced cavitation and wavefront analysis inside a water droplet. Phys. Fluids 33 (9), 097104. http://dx.doi.org/10.1063/5.0063827.

Biasiori-Poulanges, L., Schmidmayer, K., 2023. A phenomenological analysis of droplet shock-induced cavitation using a multiphase modeling approach. Phys. Fluids 35 (1), 013312. http://dx.doi.org/10.1063/5.0127105.

Bidi, S., Koukouvinis, P., Papoutsakis, A., Shams, A., Gavaises, M., 2022. Numerical study of real gas effects during bubble collapse using a disequilibrium multiphase model. Ultrason. Sonochemistry 90, 106175. http://dx.doi.org/10.1016/j.ultsonch.2022.106175.

Brennen, C.E., 2013. Cavitation and Bubble Dynamics. Cambridge University Press.

Bussonnière, A., Liu, Q., Tsai, P.A., 2020. Cavitation nuclei regeneration in a water-particle suspension. Phys. Rev. Lett. 124, 034501. http://dx.doi.org/10.1103/PhysRevLett.124.034501.

Chang, Y.J., Chang, C.H., Ho, C.C., Hsu, J.C., Kuo, C.L., 2016. Droplet-assisted laser direct nanoscale writing on silicon. Technologies 4 (1), http://dx.doi.org/10.3390/technologies4010008.

Chiapolino, A., Saurel, R., Nkonga, B., 2017. Sharpening diffuse interfaces with compressible fluids on unstructured meshes. J. Comput. Phys. 340, 389–417. http://dx.doi.org/10.1016/j.jcp.2017.03.042.

Coralic, V., 2015. Simulation of Shock-Induced Bubble Collapse with Application to Vascular Injury in Shockwave Lithotripsy (Ph.D. thesis). California Institute of Technology.

Erfanian, M., Mohammadi, A., Ebrahimi Orimi, H., Zapata-Farfan, J., Saade, J., Meunier, M., Larrivée, B., Boutopoulos, C., 2024. Drop-on-demand bioprinting: A redesigned laser-induced side transfer approach with continuous capillary perfusion. Int. J. Bioprinting 10 (3), 2832. http://dx.doi.org/10.36922/ijb.2832.

Field, J., Camus, J.J., Tinguely, M., Obreschkow, D., Farhat, M., 2012. Cavitation in impacted drops and jets and the effect on erosion damage thresholds. Wear 290–291, 154–160. http://dx.doi.org/10.1016/j.wear.2012.03.006.

Field, J.E., Dear, J.P., Ogren, J.E., 1989. The effects of target compliance on liquid drop impact. J. Appl. Phys. 65 (2), 533–540. http://dx.doi.org/10.1063/1.343136.

Forehand, R.W., Nguyen, K.C., Anderson, C.J., Shannon, R., Grace, S.M., Kinzel, M.P., 2023. A numerical assessment of shock–droplet interaction modeling including cavitation. Phys. Fluids 35 (2), 023315. http://dx.doi.org/10.1063/5.0136536.

Giannadakis, E., Gavaises, M., Arcoumanis, C., 2008. Modelling of cavitation in diesel injector nozzles. J. Fluid Mech. 616, 153–193. http://dx.doi.org/10.1017/S0022112008003777.

Godunov, S.K., Bohachevsky, I., 1959. Finite difference method for numerical computation of discontinuous solutions of the equations of fluid dynamics. Mat. Sb. 47, 271–306.

Gomez Santos, E., Shi, J., Venkatasubramanian, R., Hoffmann, G., Gavaises, M., Bauer, W., 2021. Modelling and prediction of cavitation erosion in GDi injectors operated with E100 fuel. Fuel 289, 119923. http://dx.doi.org/10.1016/j.fuel.2020.119923.

Goyal, N., Shaikh, J., Sharma, A., 2020. Bubble entrapment during head-on binary collision with large deformation of unequal-sized tetradecane droplets. Phys. Fluids 32 (12), 122114. http://dx.doi.org/10.1063/5.0029179.

Guildenbecher, D., Lopez-Rivera, C., Sojka, P., 2009. Secondary atomization. Exp. Fluids 46 (3), 371–402.

Jameson, A., Schmidt, W., Turkel, E., 1981. Numerical solution of the Euler equations by finite volume methods using Runge Kutta time stepping schemes. In: 14th Fluid and Plasma Dynamics Conference. http://dx.doi.org/10.2514/6.1981-1259.

Jiao, Y., Schmidt, S.J., Adams, N.A., 2024. Effect of gas cavity size and eccentricity on shock interaction with a cylinder at near-critical conditions. Phys. Fluids.

Johnsen, E., Colonius, T., 2009. Numerical simulations of non-spherical bubble collapse. J. Fluid Mech. 629, 231–262. http://dx.doi.org/10.1017/S0022112009006351.

Joseph, D., Belanger, J., Beavers, G., 1999. Breakup of a liquid drop suddenly exposed to a high-speed airstream. Int. J. Multiph. Flow 25 (6), 1263–1303. http://dx.doi.org/10.1016/S0301-9322(99)00043-9.

Kapila, A.K., Menikoff, R., Bdzil, J.B., Son, S.F., Stewart, D.S., 2001. Two-phase modeling of deflagration-to-detonation transition in granular materials: Reduced equations. Phys. Fluids 13 (10), 3002–3024. http://dx.doi.org/10.1063/1.1398042.

Kékesi, T., Amberg, G., Prahl Wittberg, L., 2014. Drop deformation and breakup. Int. J. Multiph. Flow 66, 1–10. http://dx.doi.org/10.1016/j.ijmultiphaseflow.2014.06.006.

Kim, Y., Hermanson, J.C., 2012. Breakup and vaporization of droplets under locally supersonic conditions. Phys. Fluids 24 (7), 076102. http://dx.doi.org/10.1063/1.4733459.

Kondo, T., Ando, K., 2019. Simulation of high-speed droplet impact against a dry/wet rigid wall for understanding the mechanism of liquid jet cleaning. Phys. Fluids 31 (1), 013303. http://dx.doi.org/10.1063/1.5079282.

Koukas, E., Papoutsakis, A., Gavaises, M., 2023. Numerical investigation of shock-induced bubble collapse dynamics and fluid–solid interactions during shock-wave lithotripsy. Ultrason. Sonochemistry 95, 106393. http://dx.doi.org/10.1016/j.ultsonch.2023.106393.

Kryou, C., Theodorakos, I., Karakaidos, P., Klinakis, A., Hatziapostolou, A., Zergioti, I., 2021. Parametric study of jet/droplet formation process during LIFT printing of living cell-laden bioink. Micromachines 12 (11), http://dx.doi.org/10.3390/mi12111408.

Kung, Y., Huang, H., Liao, W., Huang, A.P.H., Hsiao, M.Y., Wu, C.H., Liu, H.L., Inserra, C., Chen, W.S., 2020. A single high-intensity shock wave pulse with microbubbles opens the blood–brain barrier in rats. Front. Bioeng. Biotechnol..

Lee, C., Reitz, R.D., 2000. An experimental study of the effect of gas density on the distortion and breakup mechanism of drops in high speed gas stream. Int. J. Multiph. Flow 26 (2), 229–244. http://dx.doi.org/10.1016/S0301-9322(99)00020-8.

Liang, Y., Jiang, Y., Wen, C.Y., Liu, Y., 2020. Interaction of a planar shock wave and a water droplet embedded with a vapour cavity. J. Fluid Mech. 885, R6. http://dx.doi.org/10.1017/jfm.2019.1031.

Liu, N., Wang, Z., Sun, M., Wang, H., Wang, B., 2018. Numerical simulation of liquid droplet breakup in supersonic flows. Acta Astronaut. 145, 116–130. http://dx.doi.org/10.1016/j.actaastro.2018.01.010.

López López, J.M., Bakrania, A., Coupland, J., Marimuthu, S., 2016. Droplet assisted laser micromachining of hard ceramics. J. Eur. Ceram. Soc. 36 (11), 2689–2694. http://dx.doi.org/10.1016/j.jeurceramsoc.2016.04.021.

López López, J.M., Marimuthu, S., Kamara, A.M., 2017. Chapter 5 - Droplet-assisted laser cleaning of contaminated surfaces. In: Developments in Surface Contamination and Cleaning: Types of Contamination and Contamination Resources. William Andrew Publishing.

Malik, V., Salauddin, S., Patten, J., Ahmed, K.A., 2022. Exploration of RP-2 liquid droplets interaction with a detonation wave. In: AIAA SCITECH 2022 Forum. http://dx.doi.org/10.2514/6.2022-0089.

Marzbali, M., Dolatabadi, A., 2020. High-speed droplet impingement on dry and wetted substrates. Phys. Fluids 32 (11), 112101. http://dx.doi.org/10.1063/5.0020977.

Meng, J.C., Colonius, T., 2015. Numerical simulations of the early stages of high-speed droplet breakup. Shock Waves 25, 399–414.

Meng, J.C., Colonius, T., 2018. Numerical Simulation of the Aerobreakup of a Water Droplet (Ph.D. thesis). pp. 1108–1135. http://dx.doi.org/10.1017/jfm.2017.804.

Moylan, B., Landrum, B., Russell, G., 2013. Investigation of the physical phenomena associated with rain impacts on supersonic and hypersonic flight vehicles. Procedia Eng. 58, 223–231. http://dx.doi.org/10.1016/j.proeng.2013.05.026, Proceedings of the 12th Hypervelocity Impact Symposium.

Nguyen, K.C., Forehand, R., Briggs, S.M., Berube, N., Vasu, S., Kinzel, M.P., Grace, S., 2024. Onto modeling of cavitation inside a cylindrical water column exposed to high-speed shocks. In: AIAA SCITECH 2024 Forum.

Obreschkow, D., Dorsaz, N., Kobel, P., de Bosset, A., Tinguely, M., Field, J., Farhat, M., 2011. Confined shocks inside isolated liquid volumes: A new path of erosion? Phys. Fluids 23 (10), 101702. http://dx.doi.org/10.1063/1.3647583.

Papoutsakis, A., Koukouvinis, P., Gavaises, M., 2020. Solution of cavitating compressible flows using discontinuous Galerkin discretisation. J. Comput. Phys. 410, 109377. http://dx.doi.org/10.1016/j.jcp.2020.109377.

Papoutsakis, A., Nompelis, I., Ekaterinaris, J.A., 2014. Discontinuous Galerkin discretization of chemically reacting flows. In: 52nd Aerospace Sciences Meeting. http://dx.doi.org/10.2514/6.2014-0068.

Papoutsakis, A., Sazhin, S.S., Begg, S., Danaila, I., Luddens, F., 2018. An efficient adaptive mesh refinement (AMR) algorithm for the discontinuous Galerkin method: Applications for the computation of compressible two-phase flows. J. Comput. Phys. 363, 399–427. http://dx.doi.org/10.1016/j.jcp.2018.02.048.

Pelanti, M., 2022. Arbitrary-rate relaxation techniques for the numerical modeling of compressible two-phase flows with heat and mass transfer. Int. J. Multiph. Flow 153, 104097. http://dx.doi.org/10.1016/j.ijmultiphaseflow.2022.104097.

Pelanti, M., Shyue, K.-M., 2014. A mixture-energy-consistent six-equation two-phase numerical model for fluids with interfaces, cavitation and evaporation waves. J. Comput. Phys. 259, 331–357. http://dx.doi.org/10.1016/j.jcp.2013.12.003.

Rossano, V., De Stefano, G., 2025. Large-eddy simulation of droplet deformation and fragmentation under shock wave impact. Appl. Sci. 15 (3), http://dx.doi.org/10.3390/app15031233.

Saurel, R., Petitpas, F., Berry, R.A., 2009. Simple and efficient relaxation methods for interfaces separating compressible fluids, cavitating flows and shocks in multiphase mixtures. J. Comput. Phys. 228 (5), 1678–1712. http://dx.doi.org/10.1016/j.jcp.2008.11.002.

Scardina, P., Edwards, M., 2009. Chapter 1 the fundamentals of bubble formation in water treatment.

Schmidmayer, K., Biasiori-Poulanges, L., 2023. Geometry effects on the droplet shock-induced cavitation. Phys. Fluids 35 (6), 063315. http://dx.doi.org/10.1063/5.0151404.

Schmidmayer, K., Cazé, J., Petitpas, F., Daniel, E., Favrie, N., 2023. Modelling interactions between waves and diffused interfaces. Internat. J. Numer. Methods Fluids 95 (2), 215–241. http://dx.doi.org/10.1002/fld.5142.

Sembian, S., Liverts, M., Tillmark, N., Apazidis, N., 2016. Plane shock wave interaction with a cylindrical water column. Phys. Fluids 28 (5), 056102. http://dx.doi.org/10.1063/1.4948274.

Shatalov, V., Filippov, A., Noga, I., 2013. Bubbles induced fluctuations of some properties of aqueous solutions. Biophysics 57, http://dx.doi.org/10.1134/S0006350912040161.

Shatalov, V., Noga, I., Zinchenko, A., 2011. Degassing of bioliquids in low electromagnetic fields. arXiv:1105.5689.

Shpak, O., Verweij, M., De Jong, N., Versluis, M., 2016. Droplets, bubbles and ultrasound interactions. In: Escoffre, J.-M., Bouakaz, A. (Eds.), Therapeutic Ultrasound. Springer, pp. 157–174.

Song, X., Chen, G., Xu, Q., Li, B., Zhang, D., Xie, L., Wang, M., 2023a. The interaction between droplets and the vortex ring after a shock wave. Phys. Fluids 35 (6), 063331. http://dx.doi.org/10.1063/5.0151886.

Song, J., Long, T., Pan, S., 2023b. Effect of phase change on shock wave and n-dodecane droplet interaction with numerical investigation. arXiv:2306.11255.

Sun, X., Kong, D., Liang, C., Hu, Y., Duan, J.a., 2022. Flexible and precise droplet manipulation by a laser-induced shape temperature field on a lubricant-infused surface. Langmuir http://dx.doi.org/10.1021/acs.langmuir.2c00680.

Sweby, P., Baines, M., 1984. On convergence of Roe's scheme for the general non-linear scalar wave equation. J. Comput. Phys. 56 (1), 135–148. http://dx.doi.org/10.1016/0021-9991(84)90087-1.

Theofanous, T.G., 2011. Aerobreakup of Newtonian and viscoelastic liquids. Annu. Rev. Fluid Mech. 43, 661–690.

Theofanous, T.G., Li, G.J., 2008. On the physics of aerobreakup. Phys. Fluids 20 (5), 052103. http://dx.doi.org/10.1063/1.2907989.

Theofanous, T.G., Mitkin, V.V., Ng, C.L., Chang, C.-H., Deng, X., Sushchikh, S., 2012. The physics of aerobreakup. II. Viscous liquids. Phys. Fluids 24 (2), 022104. http://dx.doi.org/10.1063/1.3680867.

Toro, E.F., 2013. Riemann Solvers and Numerical Methods for Fluid Dynamics: A Practical Introduction. Springer Science & Business Media.

Viqueira-Moreira, M., Dworzanczyk, A., Parziale, N.J., Brehm, C., 2023. Numerical investigation of droplet aerobreakup and impingement experiments at mach 5. In: AIAA AVIATION 2023 Forum. http://dx.doi.org/10.2514/6.2023-4251, arXiv:https://arc.aiaa.org/doi/pdf/10.2514/6.2023-4251.

Wei, Y., Dong, R., Zhang, Y., Liang, S., 2023. Study on the interface instability of a shock wave–sub-millimeter liquid droplet interface and a numerical investigation of its breakup. Appl. Sci. 13 (24), http://dx.doi.org/10.3390/app132413283.

Wierzba, A., Takayama, K., 1988. Experimental investigation of the aerodynamic breakup of liquid drops. AIAA J. 26 (11), 1329–1335. http://dx.doi.org/10.2514/3.10044.

Wijngaarden, L.v., 2007. Shock waves in bubbly liquids. In: Dongen, M.E.H.v. (Ed.), Shock Wave Science and Technology Reference Library: Multiphase Flows I. Springer Berlin Heidelberg, Berlin, Heidelberg, pp. 3–33. http://dx.doi.org/10.1007/978-3-540-35846-6_1.

Xiong, T., Shao, C., Luo, K., 2024. Exploration of shock–droplet interaction based on high-fidelity simulation and improved theoretical model. J. Fluid Mech. 988, A46. http://dx.doi.org/10.1017/jfm.2024.472.

Xu, S., Fan, W., Wu, W., Wen, H., Wang, B., 2023. Analysis of wave converging phenomena inside the shocked two-dimensional cylindrical water column. J. Fluid Mech. 964, A12. http://dx.doi.org/10.1017/jfm.2023.239.